

Modeling lower mantle anisotropy development in a subducting slab

H.-R. Wenk^{a,*}, S. Speziale^a, A.K. McNamara^b, E.J. Garnero^b

^a *Department of Earth and Planetary Science, University of California, Berkeley, California 94720, USA*

^b *Department of Geological Sciences, Arizona State University, Tempe, Arizona 85287, USA*

Received 31 August 2005; received in revised form 28 January 2006; accepted 16 February 2006

Available online 5 April 2006

Editor: S. King

Abstract

A model is presented that simulates anisotropy development in a subducting slab from the upper–lower mantle boundary (661 km) to the core–mantle boundary (2891 km). Two phases are considered: orthorhombic MgSiO₃-perovskite and cubic magnesiowuestite (Mg,Fe)O. Single crystal elastic properties at mantle conditions are obtained from existing density functional theory calculations and quasiharmonic approximation. It is assumed that deformation is accommodated by slip. A polycrystal plasticity model predicts strong texture development for perovskite and weaker texture for magnesiowuestite. When averaging single crystal elastic properties with the orientation distribution this results for both phases in weak P-wave anisotropy and shear wave splitting in the upper part of the lower mantle but pronounced anisotropy near the core–mantle boundary (up to 4% for V_p and 7% for V_s). The anisotropy pattern is complex and asymmetric and local heterogeneity is expected. These predictions are consistent with seismic observations.

© 2006 Elsevier B.V. All rights reserved.

Keywords: lower mantle; anisotropy; texture; elasticity; perovskite; magnesiowuestite

1. Introduction

In many parts of the earth seismologists have established that seismic waves travel at different velocities in different propagation directions. This is the case in large parts of the upper mantle [1,2], in the lowermost few hundred kilometers of the mantle (the D'' layer) [3,4] and in the inner core [5,6]. In the upper mantle such anisotropy is best understood and has been related to preferred orientation of olivine that was attained during convection [2,7,8]. This interpretation relies on a detailed knowledge of microscopic deforma-

tion mechanisms, the effects of these mechanisms on reorientation of crystals in a macroscopic deformation field, and on the elastic properties of single crystals at given temperature–pressure conditions.

For the upper mantle, where parameters are best defined from experiments, linked micro–macro scale simulations have been successful in predicting realistic seismic anisotropy and relating it to the convection pattern induced by a temperature gradient [9,10]. Similar simulations for the inner core are much more hypothetical [11].

Little is known about local anisotropy in the lower mantle that composes most of Earth's volume and may be of great geodynamical importance for processes that occur near the surface [12,13]. Conditions in the lower

* Corresponding author.

E-mail address: [wenz@seismo.berkeley.edu](mailto:wenk@seismo.berkeley.edu) (H.-R. Wenk).

mantle are beyond ordinary deformation experiments and knowledge about deformation mechanisms is highly speculative. Also, seismic coverage is very incomplete, leading to assumptions that lack of evidence for anisotropy must indicate diffusion creep or superplasticity [14–17].

In this paper we present a first quantitative model for anisotropy development that relies on physical principles and incorporates recent advances in elasticity and plasticity for perovskite and magnesiowuestite at high pressure. We are fully aware of the limitations in the three main ingredients of the model, (a) the macroscopic deformation field as established by geodynamics, (b) microscopic deformation mechanisms, particularly intracrystalline slip systems and (c) elastic properties of single crystals. We will address those limitations in detail in later sections. But with many recent advances on all three of these issues we venture a first attempt to simulate anisotropy development in the lower mantle in a subducting slab. While uncertainties may prevent direct application of results to any specific location, they nevertheless give realistic magnitudes of anisotropy that can be expected in a convecting lower mantle and the model is easily expanded as new information becomes available.

2. Ingredients

2.1. Geodynamic model

For this work, we use deformational information derived from the two-dimensional geodynamical model put forth by McNamara et al. [18] which is representative of a suite of possible parameter sets [19]. This model investigates the deformational characteristics of a subducting slab descending through the lower mantle and coming into contact with the core mantle boundary. It should be noted that this model is isochemical, in contrast to thermochemical mantle models which employ a thin dense mantle component at the base of the mantle [e.g. 20–24]. However, these thermochemical studies indicate that a possible denser component is expected to be swept away from subducting slabs, therefore, the isochemical assumption [22] is expected to be valid in downwelling regions.

Details of the geodynamical model and method are found in McNamara et al. [18,19], and only a brief summary is given here. The geodynamical model uses a composite rheology consisting of both dislocation creep which promotes the development of lattice preferred orientation (texture) and diffusion creep which may randomize mineral fabrics. Viscosity parameters were

derived from mineral physics experiments [25]. Lagrangian tracers were utilized to track the deformational properties of the slab. Dislocation creep induced strain in subducting slabs was calculated. In these first studies, strain was used as a measure for fabric development without using detailed intracrystalline mechanisms. It was found that subducting slabs are under high stress and are likely to flow by dislocation creep. Dislocation creep induced strain within slabs builds up slowly in the upper portion of the lower mantle and sharply increases as slab material approaches the lowermost mantle. The resultant strain patterns were similar for several cases in which rheological parameters were varied within mineral physics constraints, indicating that deformational characteristics are not highly sensitive to the precise rheological formulation. This new work is quite different in that fabric development is simulated based on intracrystalline deformation mechanisms and the deformation history and anisotropy is calculated from the texture patterns that evolve.

Deformational parameters from the tracer are used to define the deformation history. The representative Lagrangian tracer is positioned in a subducting slab (sketched in Fig. 1). Deformation is recorded for 5000 time steps as the tracer descended from 700 to 2760 km depth (Fig. 2). At mid-lower mantle depths, the tracer had brief temporal excursions into the diffusion creep regime resulting in a discontinuous record of strain. To overcome problems associated with applying discontinuous deformation parameters at these depths to the

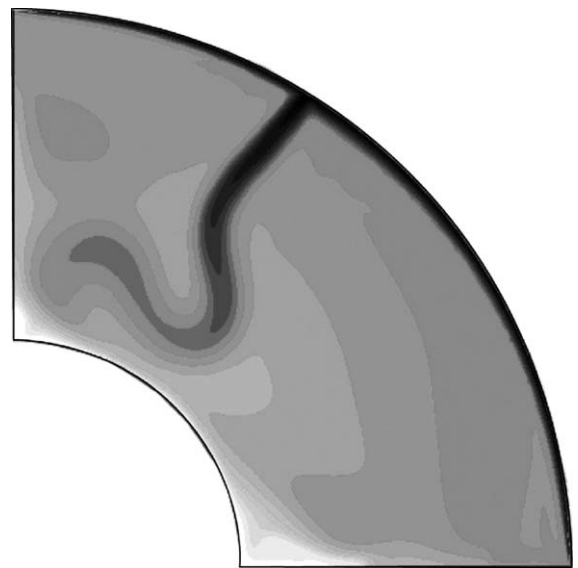


Fig. 1. Snapshot of the temperature field from the convection calculation from which the Lagrangian tracer's streamline was taken from. Gray shades give relative temperature (dark: cold, light: hot).

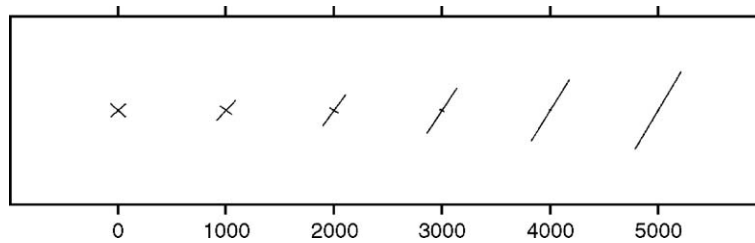


Fig. 2. Strain evolution along a streamline in a subducting slab recorded by a tracer. Maximum and minimum stretch of the Lagrangian particle as a function of timestep [18]. The core–mantle boundary surface is horizontal.

texture models, we assume a constant deformation for depths greater than 2300 steps. For the tracer particle, which is close to the center of the subducting slab, we obtain a total von Mises strain of 2.5 near the core–mantle boundary.

2.2. Deformation mechanisms

In our model we assume that deformation was accommodated by slip. It is conceivable that other mechanisms occur during lower mantle deformation, particularly if diffusion is significant. Superplasticity, typical of fine-grained materials near the melting point, has been suggested as a possibility [25,26]. This mechanism generally does not produce preferred orientation as long as grains are equiaxed. Also climb and recovery associated with slip do not contribute to orientation changes. Dynamic recrystallization may occur and either strengthen or weaken existing crystal orientation patterns [27,28]. Since we assume dislocation glide as mechanism and homogeneous deformation, the predicted texture strengths may be close to the maximum that can be expected for the envisioned subduction geometry.

While deformation of the upper mantle is reasonably constrained by experiments, even novel high pressure apparatus such as rotational Drickamer [25] or multi-anvil [29] only extend to pressure conditions of the transition zone. For pressures corresponding to the lower mantle, radial X-ray diffraction experiments in the diamond anvil cell [30] are presently the main experimental method to obtain information about deformation mechanisms.

Slip systems of magnesiowüstite (Fe,Mg)O and periclase (MgO) have been investigated at intermediate to high pressures. At high pressure and low temperature $\{110\}\langle\bar{1}\bar{1}0\rangle$ is the dominant slip system [31,32], at intermediate pressure and high temperature $\{111\}\langle\bar{1}\bar{1}0\rangle$ and $\{001\}\langle\bar{1}\bar{1}0\rangle$ become active [33–35]. This is analogous to isostructural halite [36] and for the simulations it is assumed that at temperatures of the

lower mantle all slip systems are potentially active (Table 1). Even though we assign a lower critical shear stress to $\{110\}$, the most active system in the polycrystal is $\{111\}$ due to symmetry multiplicity. Mechanisms for periclase and magnesiowüstite appear to be similar [33]. Recent theoretical estimations of Peierl's stresses confirm the experimental results that increasing pressure favors the $\{110\}$ system [37].

Much less is known about magnesium perovskite. From experiments on analog materials with similar structures a variety of slip systems and deformation mechanisms have been proposed, including (010)[100], (100)[010], (001)[100] and (001) $\langle\bar{1}10\rangle$ (in orthorhombic setting, Table 1) [26,38–42]. Inferences from analogs, particularly if they are of different symmetry (cubic rather than orthorhombic), are unreliable as numerous examples testify (e.g. zinc–zirconium, calcite–magnesite), but compression of MgSiO_3 perovskite in large volume press apparatus at lower mantle pressure produced dislocations that are consistent with the slip systems listed above [43].

The conclusions are also supported by recent deformation experiments in diamond anvil cells at lower mantle pressure that produced texture patterns in MgSiO_3 perovskite [44,45]. A variety of texture types were observed but the most common one has [001] axes nearly parallel to the compression direction as is illustrated in an inverse pole figure (Fig. 3a). Assuming deformation by dislocation glide and activity of the slip systems in Table 1 a pattern is simulated that closely matches the experiment (Fig. 3b). It is noteworthy that all experimental textures for perovskite are strongly

Table 1

Slip systems and critical resolved shear stress coefficients assumed in the polycrystal plasticity simulations

Perovskite		Magnesiowüstite	
(010)[100]	1	$\{111\}\langle\bar{1}0\bar{1}\rangle$	1
(100)[010]	1	$\{110\}\langle\bar{1}\bar{1}0\rangle$	0.8
(001) $\langle\bar{1}10\rangle$	1	$\{100\}\langle\bar{0}11\rangle$	1
(001)[100]	1		

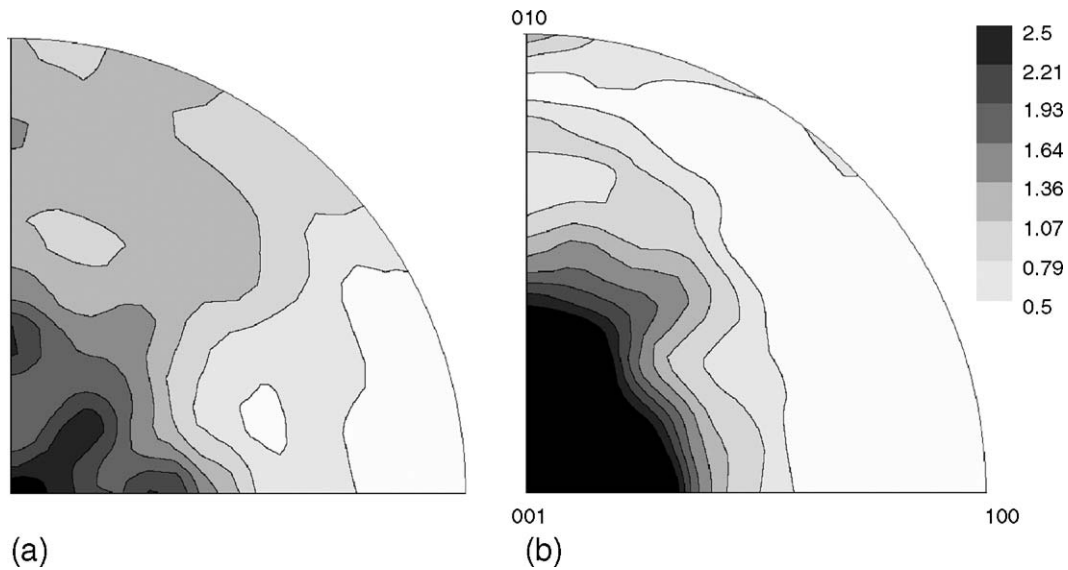


Fig. 3. Texture development in perovskite deformed in axial compression. Inverse pole figures of the compression direction, equal area projection, linear contours in multiples of a random distribution (m.r.d.). (a) Radial diamond anvil cell experiment. Perovskite transformed from enstatite and compressed to 42 GPa. (b) Texture simulation for slip systems listed in Table 1 [45].

orthorhombic (and not cubic), consistent with calculations suggesting that the orthorhombic character of structure and elasticity increases with pressure [46–48]. Admittedly, these experiments were all performed at room temperature and high stresses, far from conditions prevailing in the lower mantle. At this point we can only speculate about the effect of temperature, though in the future *ab initio* calculations may allow extrapolations. As in the case of MgO it is expected that at high temperature potential slip systems are activated more equally. Increasing pressure may have a similar effect on critical shear stresses as decreasing temperature. A similar tendency is true for volume changes (and for compressional moduli), thermal vibration and bonding. For MgSiO₃ perovskite the temperature relative to the melting point does not change very much along the geotherm. Based on experimental results about the melting temperature of (Mg,Fe)SiO₃ and MgSiO₃ [49,50], the homologous temperature (T/T_{Melting}) of MgSiO₃ along the cold geotherm used in our calculation changes from 0.49 ± 0.01 to 0.59 ± 0.04 . In the polycrystal simulations we assume that all four potential slip systems are active and have the same critical shear stress coefficient (Table 1) but we find that (001)<110> slip is most active.

In addition to slip systems the relative strength of the contributing phases is important. High temperature experiments on MgSiO₃ perovskite suggest that this phase is considerably stronger than MgO and this could have a significant effect on the rheology [51]. We will

discuss this issue further in the section on polycrystal plasticity simulations.

2.3. Elastic properties

Elastic properties of the minerals of the lower mantle have been the subject of both experimental and computational studies and there are considerable discrepancies between results of different approaches.

There are only two experimental measurements of the elastic constants of MgO at simultaneous high pressure and high temperature [52,53]. Mixed derivatives $\partial M / \partial P \partial T$ (where M represents the elastic modulus) retrieved in these two studies either disagree in sign (in the case of the individual elastic constants C_{11} , C_{44} , and the bulk modulus K), or their values differ by an order of magnitude (as in the case of C_{12} and the shear modulus G). In addition, these measurements are restricted to small pressure and temperature ranges, far removed from lower mantle conditions. There are several high pressure studies up to 50 GPa at room temperature [54–57] and high temperature studies at ambient pressure [58]. Even though the results at ambient conditions agree between the different studies within 1% for all the constants, the individual pressure derivatives differ up to 15% for both bulk and shear modulus when extrapolated to pressures characteristic of the deep lower mantle.

The single-crystal elasticity data available for MgSiO₃ perovskite are limited to two complete sets of

Table 2

Single crystal elastic constants of periclase [64] and magnesium silicate perovskite [48] along lower mantle geotherm from density functional theory and lattice dynamics in quasiharmonic approximation

Depth (km)	661	952	1304	1764	2270	2757
Pressure (GPa)	23.4	36.4	52.7	75	101.2	127.9
Temperature (K)	1737	1919	2143	2391	2634	2841
Temperature (°C)	1464	1646	1870	2118	2361	2568
MgO						
Density (10^3 g/m^3)	3.862	4.046	4.256	4.508	4.75	4.978
C_{11} (GPa)	428.8	532.8	657.1	821.0	1008.6	1197.9
C_{12} (GPa)	133.0	151.0	173.0	201.7	233.4	264.2
C_{44} (GPa)	153.2	162.2	171.4	181.5	191.5	200.6
MgSiO ₃ -perovskite						
Density (10^3 g/m^3)	4.357	4.506	4.69	4.929	5.165	5.375
C_{11} (GPa)	543.9	597.0	652.4	720.1	802.8	895.1
C_{12} (GPa)	219.6	265.7	319.0	389.9	477.1	567.0
C_{13} (GPa)	207.2	240.8	281.6	334.6	392.5	457.1
C_{22} (GPa)	606.5	676.4	756.2	862.3	990.9	1127.0
C_{23} (GPa)	226.9	261.9	303.5	357.9	422.7	489.9
C_{33} (GPa)	567.4	648.5	735.7	846.2	974.9	1106.3
C_{44} (GPa)	191.5	208.9	229.3	255.0	282.5	313.1
C_{55} (GPa)	181.9	193.8	205.2	220.1	240.2	259.2
C_{66} (GPa)	161.7	182.9	206.1	235.2	267.0	299.4

elastic constants at ambient conditions [59,60] which show differences up to 13% for the individual constants, and 4% and 1% for the aggregate bulk and shear moduli. Pressure and temperature dependence of the aggregate moduli K and G of MgSiO₃ perovskite have been determined by ultrasonic interferometry on polycrystalline samples [61–66]. The results of these studies are in substantial agreement, but they are limited to 9 GPa and 900 K.

Single crystal elastic constants have been calculated by various authors for both MgO and MgSiO₃ at lower mantle condition by density functional theory using different theoretical approaches for the thermal effects. In a series of studies the quasiharmonic approximation was used to calculate the thermal contribution to free energy for MgO and MgSiO₃ respectively [48,62,64]. In two studies a more rigorous ab initio molecular dynamics approach was used for MgSiO₃-perovskite [46,47] which directly takes into account anharmonic effects [65]. The results of these different approaches for MgSiO₃ are similar (see for instance [48]), with an average 2% difference for the compressional constants (C_{11} , C_{22} , C_{33}), 1% difference for the off-diagonal constants (C_{12} , C_{13} , C_{23}), and 10% difference for the shear constants (C_{44} , C_{55} , C_{66}) through wide pressure and temperature ranges (38–88 GPa, 1500–3500 K). The agreement between the different techniques is especially good in terms of averaged elastic moduli, K and G (0.9% and 2.5% respectively) as also independently confirmed by a

self-consistent thermodynamic approach [66]. The differences are smaller than other uncertainties of the model.

Here we use theoretically derived elastic properties for both minerals, rather than results from experimental studies, which cover a limited pressure and temperature range, the available pressure and temperature derivatives are often in disagreement and this causes large uncertainties in the extrapolations to deep mantle conditions. We chose the results from Karki et al. [64] for MgO and Wentzkovitch et al. [48] for perovskite because of their extensive pressure and temperature coverage. The calculated elastic properties of the two minerals along the lower mantle geotherm are listed in Table 2.

From elastic properties we calculated P and S-wave velocity surfaces, including shear-wave splitting and corresponding anisotropies. Periclase (MgO) displays at ambient conditions a single-crystal P-wave anisotropy of 11% (defined as $100 \times (V_{P\max} - V_{P\min}) / V_{P\text{avg}}$, where $V_{P\text{avg}}$ is $1/2(V_{P\max} + V_{P\min})$). The shear-wave splitting anisotropy (ΔV_S , defined as $100 \times \max(V_{S1} - V_{S2}) / (V_{S\text{avg}})$ where $\max(V_{S1} - V_{S2})$ is the maximum value of

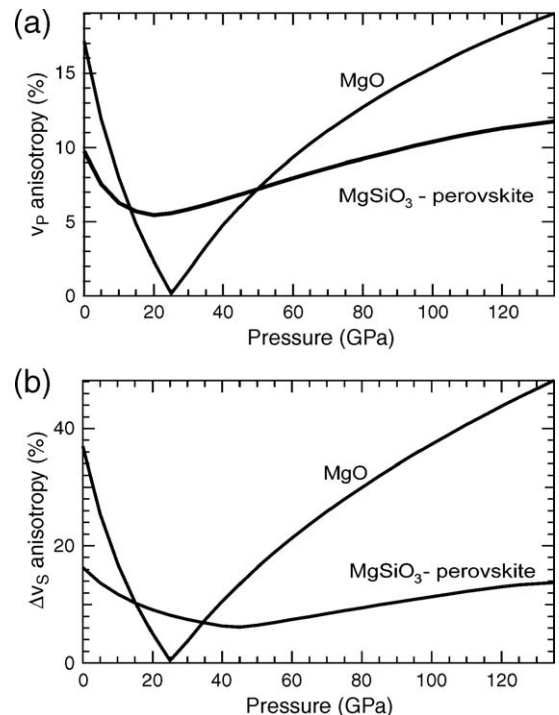


Fig. 4. (a) Single crystal P-wave anisotropy and (b) ΔS anisotropy for the two main lower mantle minerals periclase MgO and perovskite MgSiO₃ with depth along a cold mantle geotherm based on first principles calculations [48,64].

the difference between the two polarizations of the S-velocity along the same direction of propagation, and V_{Savg} is $1/2(V_{\text{Smax}} + V_{\text{Smin}})$ is 21%. Along the mantle geotherm, periclase becomes isotropic at 28 ± 2 GPa, with inversion of fast and slow compressional velocity directions between [111] and [100]. The fast and slow shear polarization directions switch from [100] and [110] at the same pressure (Fig. 4). P-wave velocity anisotropy and ΔS anisotropy steadily increase to 19% and 48% at the base of the lower mantle, based on theory (Fig. 4).

The single crystal P-wave velocity surfaces (normalized so that the maximum value is 100%) of MgO at five different depths are shown in Fig. 5a and that for shear wave splitting ΔS in Fig. 5c (normalized to express ΔS in % of the average S-wave velocity). At depth the fastest P-wave is along $\langle 100 \rangle$ and the largest splitting along $\langle 110 \rangle$. At ambient conditions 10–20 mol% Fe

substitution for Mg slightly decreases the elastic anisotropy of magnesiowuestite [67].

Magnesium silicate perovskite is metastable at ambient conditions [68]. Experiments at ambient conditions suggest 8% P-wave anisotropy and 15% shear-wave splitting anisotropy [52]. Quasiharmonic calculations [48] suggest that P-velocity anisotropy increases along the lower mantle geotherm to 12% and ΔS anisotropy first decreases to 5% at 40 GPa and then increases to 14% at the core–mantle boundary (Fig. 4). Comparing ab initio calculations [46–48] we estimate uncertainties of about 10% and 25% for P-wave anisotropy and S-wave splitting anisotropy at depth. The normalized single crystal P- and ΔS - surfaces for perovskite are shown in Fig. 5b and d respectively. The P-waves are fast along [010] (or more precisely [0.4 1 0]) and slow along [100]; ΔS is strong along [110] (or more precisely [1 1 0.4]) (up to 14%). Notice the strong

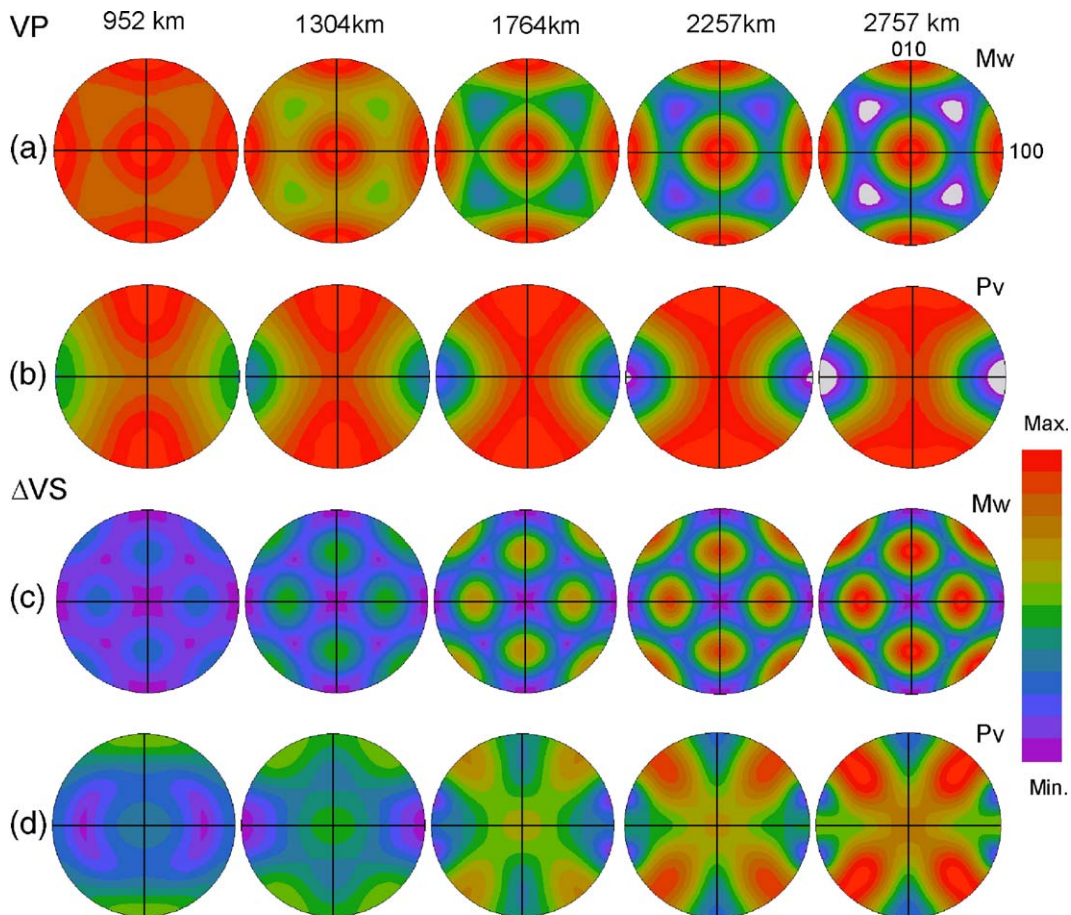


Fig. 5. Normalized single crystal surfaces for P-wave (a,b) and ΔS anisotropy (c,d) evolution along a streamline with depth. (a,c) periclase MgO (Mw) [64], (b,d) perovskite MgSiO₃ (Pv) [48]. Equal area projection, linear contours with color patterns indicated. Minimum and maximum on the color scale are: (a) 85–100%, (b) 90–100%, (c) 0–27%, (d) 0–9%.

orthorhombic nature of the pattern. The effect of 10–20 mol% Fe substitution for Mg on anisotropy investigated by quasiharmonic calculations is minimal [69]. The recently observed high- to low-spin transition in magnesiowuestites and Fe–Mg silicate perovskites [70,71] may complicate the picture of elastic properties of these minerals [72].

3. Polycrystal plasticity model and results

Texture development along a streamline model for a subducting slab (Figs. 1,2 [18]) was simulated with the tangent approximation of the viscoplastic self-consistent model, implemented in the Los Alamos VPSC code [73]. This polycrystal plasticity model relies on the concept of grain inclusions in a homogeneous but anisotropic medium and is intermediate between the Taylor model that enforces strain compatibility and the Sachs model that is based on equilibrium. The model does not take grain interaction or intragranular heterogeneity into account and is thus still a simplification of real processes but the VPSC approach has been reliable in simulating textures of many low symmetry materials [74]. The system under consideration consists of two phases, a major phase perovskite (70 vol.%) and a minor phase magnesiowuestite (30 vol.%). It is likely that perovskite has higher critical shear stresses than magnesiowuestite under most conditions [51]. The VPSC code has been applied to multiple phases [75] but results for multiphase composites can be unrealistic because of local heterogeneities. Sophisticated finite element models that would allow for boundary processes do not exist and neither do experimental data to provide information about grain interaction. We used two approaches in the VPSC calculations: First we simulated deformation of a two-phase composite [75] and then for each phase individually, adjusting for volume fractions in the strain contribution.

The second case is more useful because we can then assess the effects if one of the phases, or both phases of the aggregate develops texture. This way we can also make better use of grain statistics. Among several scenarios two may occur: The weak phase may segregate into layers as quartz in granitic mylonites and deformation may concentrate on these layers, developing shear bands. Alternatively the weak subordinate phase may concentrate in pockets at grain boundaries and deform heterogeneously without much texture. When the grains of the dominant hard phase make contact, they will dominate the deformation, as in some peridotites. In diamond anvil experiments at room

temperature perovskite and magnesiowuestite both deform and develop textures but magnesiowuestite textures are very weak [44].

In the simulations 2000 grains were deformed in 5000 steps, starting at the upper–lower mantle boundary (661 km) and proceeding towards the core–mantle boundary (maximum depth 2757 km). It was assumed that during transformations from spinel structures to perovskite and magnesiowuestite at the base of the transition zone orientations were randomized. Each deformation step was defined by a displacement gradient tensor obtained from the tracer geometry of the geodynamic model. A viscoplastic strain-rate sensitive flow law with a stress exponent $n=3$ was used. Activity of slip systems in all 2000 grains is evaluated in each of the 5000 orientation steps and orientations are updated accordingly. From the orientation distribution of 2000 grains, pole figures were calculated to illustrate crystal orientation patterns. Aggregate elastic properties were calculated, using a geometric mean [76]. All texture-related calculations have been performed with the software Beartex [77].

Texture patterns are shown as pole figures (Fig. 6a,b) in the same orientation as the streamline in Fig. 2 with V indicating the vertical and H the horizontal direction. Color shades display orientation densities. Red regions are characterized by high densities, green regions correspond to densities close to those of a random distribution, and blue and white regions are deficient in orientations. The five columns in Fig. 6 correspond to 1000 steps (952 km, 36.4 GPa, 1646 °C), 2000 steps (1304 km, 52.7 GPa, 1870 °C), 3000 steps (1764 km, 75.0 GPa, 2118 °C), 4000 steps (2270 km, 101.2 GPa, 2361 °C) and 5000 steps (2757 km, 127.9 GPa, 2568 °C). All pole figures have monoclinic symmetry consistent with the plane strain deformation history. The (100) pole figures for magnesiowuestite (Fig. 6a) illustrate that a distinct pattern develops after 2000 steps. The texture continues to strengthen moderately, with maxima up to 3.5 multiples of a random distribution (m.r.d.) after 5000 steps. For perovskite (Fig. 6b) (001) pole figures show already a strong texture after 2000 steps; the texture continues to strengthen to 40 m.r.d. after 5000 steps. The texture patterns are oblique with respect to earth coordinates because of the contribution of simple shear deformation along the streamline.

Normalized aggregate P-velocity surfaces and ΔS anisotropy surfaces, calculated by averaging single crystal elastic properties over all orientations at corresponding pressure temperature conditions for magnesiowuestite are shown in Fig. 7a,c and for

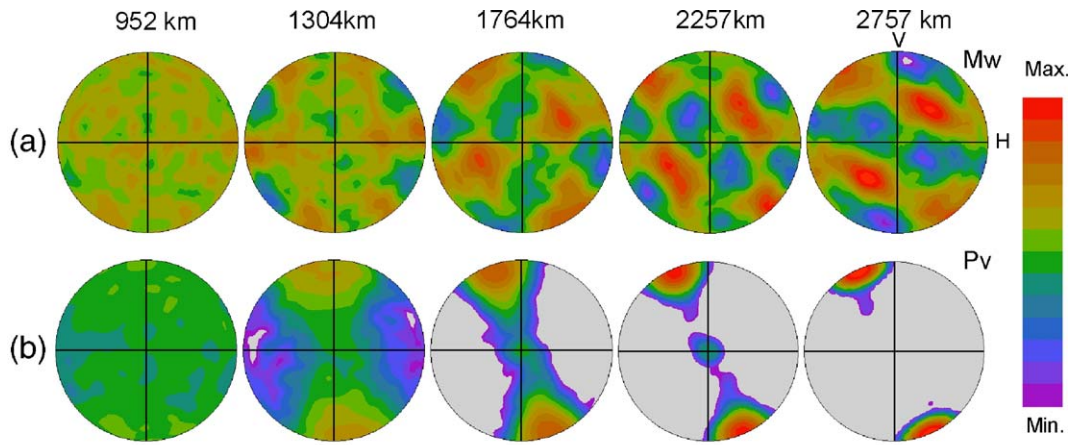


Fig. 6. Texture evolution along a streamline with depth. (a) (100) pole figures for magnesiowuestite, (b) (001) pole figures for perovskite. Equal area projection with top corresponding to the vertical direction and horizontal plane corresponding to the core–mantle boundary plane. Logarithmic contours with minimum and maximum on the color scale (a) 0.2–3.5 multiples of a random distribution (m.r.d.), (b) 0.2–40 m.r.d.

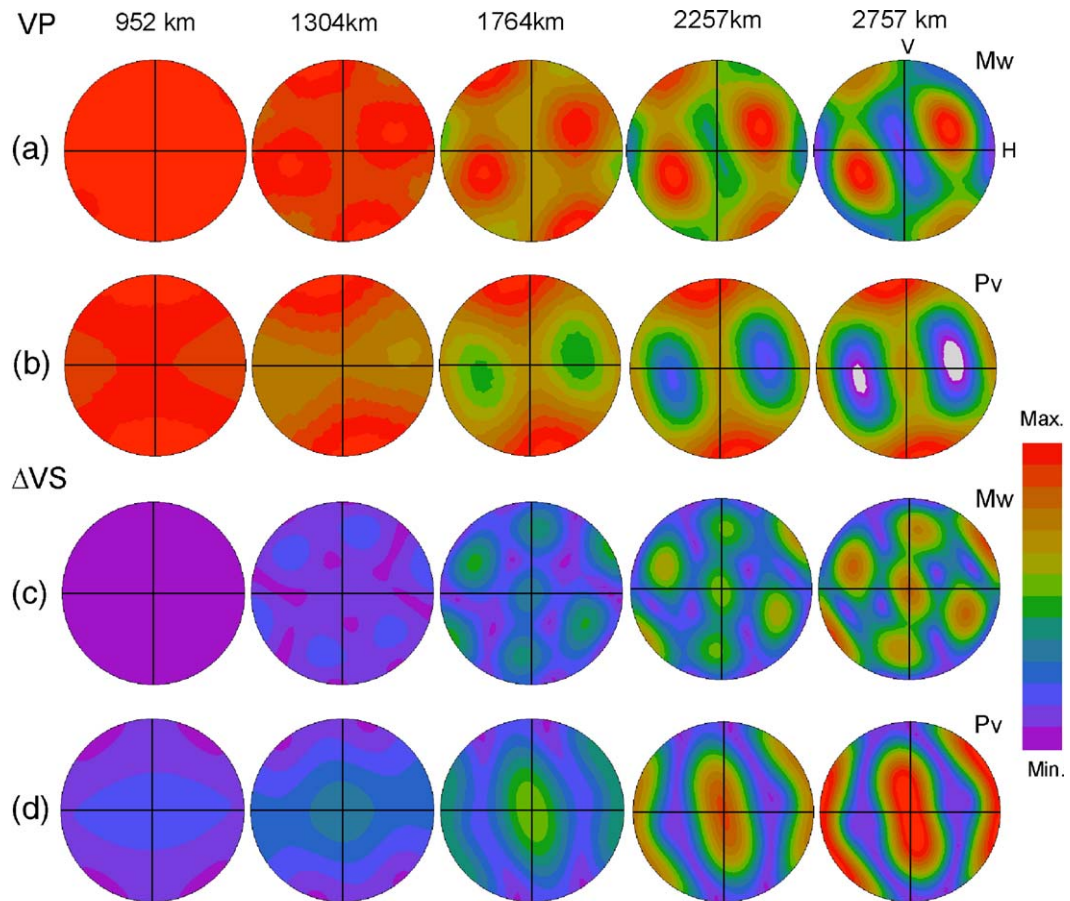


Fig. 7. Normalized aggregate surfaces for P-wave (a,b) and ΔS anisotropy (c,d) evolution along a streamline with depth. (a,c) Magnesiowuestite (Mw), (b,d) perovskite (Pv). Same coordinates as Fig. 6. Equal area projection, linear contours with color patterns indicated. Minimum and maximum on the color scale are (a,b) 96–100%, (c,d) 0–7%.

perovskite in Fig. 7b,d. For both minerals anisotropy increases with depth such that at the bottom of the lower mantle P-wave anisotropy and ΔS anisotropy reach values of 4% and 7% for both magnesiowuestite and perovskite. For this particular texture pattern the magnesiowuestite P-velocity surface is nearly opposite to that of perovskite; thus in a mixture in which both phases develop texture the anisotropy would be reduced to about 3%. The largest shear-wave splitting of the two minerals is in similar directions.

4. Discussion

We have simulated texture and anisotropy development in a slab that is subducted into the lower mantle for the two main likely phases, perovskite and magnesiowuestite. The results suggest that, if part of the deformation is accommodated by dislocation glide, strong textures develop in perovskite and more moderate textures in magnesiowuestite. The texture strength increases with depth and the pattern is asymmetric relative to earth coordinates due to significant simple shear. Single crystal elastic anisotropy also increases with depth, according to *ab initio* computational results. Due to these combined contributions, anisotropy is weak in the upper part of the lower mantle and becomes more pronounced with depth. Of course aggregate anisotropy can never exceed that of the single crystal. Due to the moderate and complex single crystal P-wave anisotropy of perovskite (12%), even strong textures do not produce strong aggregate anisotropy. This is different from olivine, the main component of the upper mantle, where P-wave propagation along [100] is 25% faster than along the [010] direction [78]. The model predicts that anisotropy varies both laterally and with depth. Of particular significance for seismology is that texture (and anisotropy) patterns are oblique and thus are most likely invisible in any seismic reconstruction that relies on transverse averaging.

We reemphasize that perovskite and magnesiowuestite were treated as separate phases to best permit evaluation of their relative deformation. Isotropic finite element simulations with no change in grain topology [79] indicate that at large strains both phases deform, with the dominant phase perovskite forming a framework and magnesiowuestite in heterogeneous pockets along grain boundaries.

It is appropriate to compare simulations with seismic observations and explore if they are compatible or not. For some time, seismologists observed shear wave anisotropy in the lowermost few hundred kilometers of

the mantle, the D'' region [e.g. 3,4,80,81]. This anisotropy is typically mapped at the level of 1–3% [82], but most commonly near the 1–1.5% range [83–85]. Evidence for lower mantle anisotropy has been mainly under past or present subduction or upwelling regions, which has resulted in proposing geodynamical mechanisms that invoke crystal preferred orientation in giving rise to the observed seismic shear wave splitting [22,23]. One region (beneath the central Atlantic) that appears neither associated with past subduction nor upwelling has been mapped as lacking D'' anisotropy [86]. In comparison to the upper mantle [1,2], deep mantle anisotropy is generally much weaker in magnitude. Anisotropy in the range of 1–3% is compatible with the predictions of our model and could thus be attributed to preferred orientation of magnesiowuestite and perovskite. Conceivably anisotropy could be enhanced if a postperovskite phase is present [87] with a larger single crystal elastic anisotropy [88]. We have excluded this phase from our model because it would only apply to the very deepest part of the subducting slab [89]. Also recent studies indicate that the seismic anisotropy contribution of postperovskite in an aggregate may be minor [90] but this should be further investigated in the future.

One challenge in mapping anisotropy in the lower mantle is constraining its depth distribution. Two seismic phases are the main deep mantle anisotropy probes: the core-reflected ScS wave, and the core-grazing S wave (or diffracted S_{diff} see Fig. 8). ScS does not have the ability to constrain anisotropy depth distribution, since it is commonly far away from the phase it is referenced to, the more shallowly bottoming direct S wave (Fig. 8a). The role of the direct S wave at epicentral distances greater than 85° changes from being the reference phase of ScS to the D'' anisotropy probe, as it penetrates to D'' depths at these distances. This probe is referenced to the SKS arrival, which arrives too close in time to the S wave to make reliable shear wave splitting measurements at distances smaller than around 90°. It greatly reduces our ability to constrain the depth distribution of lower mantle anisotropy (if present) in the several hundred km above the D'' layer. However, there are some observations where the S wave is predicted to bottom above the D'' layer that suggest anisotropy. For example, SKS and S data are shown in Fig. 8b, where shifts in the onsets of the direct S wave between the SH (dotted) and SV (solid) component are visible at distances less than 90°. Recordings at distances less than around 88° theoretically turn at depths above a 300 km thick D'' layer, thus should not contain shear wave splitting in an isotropic lower mantle. In some cases, splitting of the S wave

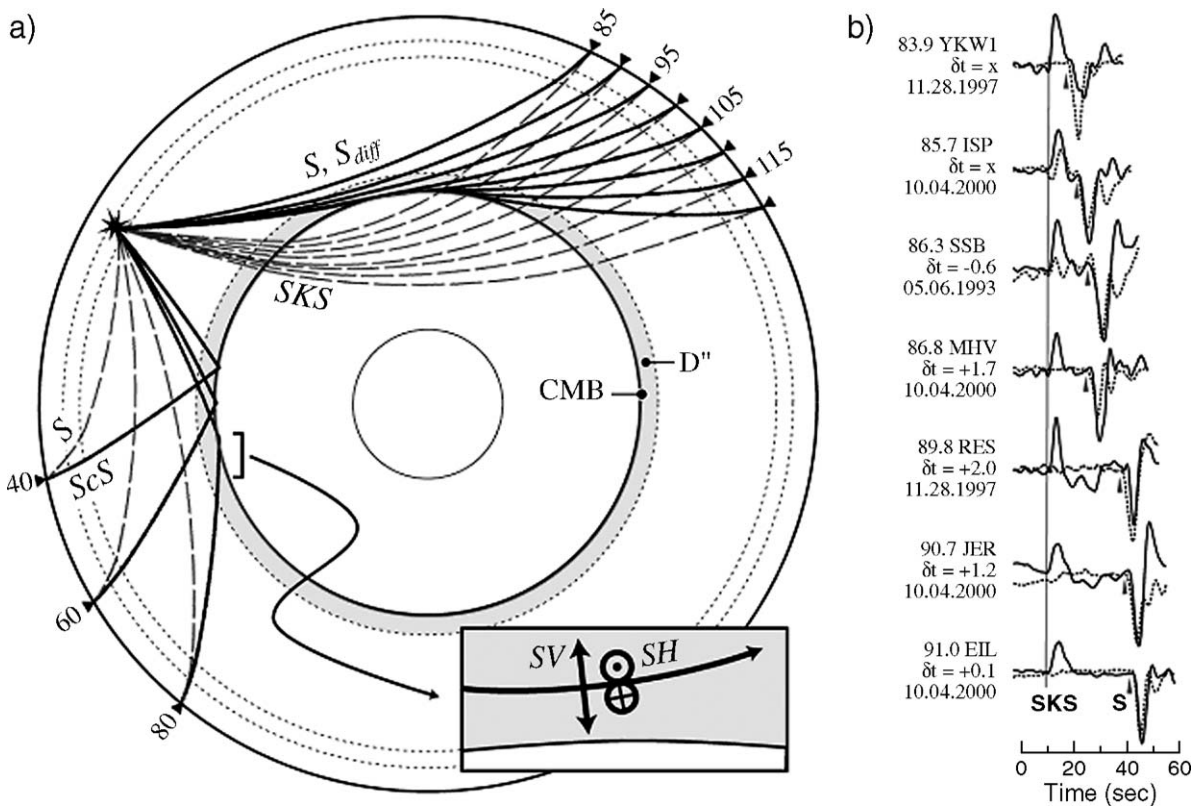


Fig. 8. (a) Ray paths of two main seismic probes for mapping lower mantle anisotropy: ScS (lower left), which is referenced to the direct S-wave, and at larger distances, S (then S_{diff}), which is referenced to SKS. The latter has greatest potential for mapping the depth distribution of deep mantle anisotropy, but is challenged by the close proximity in time to its reference SKS wave, as shown in (b) for examples of real data. SV (solid) and SH (dashed) traces are shown for seven seismogram pairs. Information to left of data indicate epicentral distance in degrees, seismographic station name, shear wave splitting time (if measurable), and earthquake date (mm.dd.yyyy).

cannot be confidently assessed, due to proximity of the tail of SKS. These data have been corrected for predictions of upper mantle anisotropy at the seismic receivers. One challenge, as seen for the 85.7° distance record at station ISP, is that upper mantle anisotropy corrections are not always successful at removing the SKS phase from the tangential component seismogram. This introduces significant uncertainty on any D'' shear wave splitting for such data. The four largest distance data in the Figure show much better SKS correction, in that SKS energy is typically absent from the corrected SH component. Anisotropy in the rest of Earth's lower mantle, e.g., roughly 700–2500 km depth, is unconstrained in traditional deep mantle anisotropy analyses, though it would be expected to see significant S wave splitting for mid-lower mantle S waves, which has not been reported to date.

Mapping the depth extent of anisotropy in the deep mantle is important, especially in the vicinity of subducted material. As we expect high strains in the

deepest mantle beneath subduction [18] may give rise to locally heterogeneous fabric development, high resolution seismic mapping could document such variations. Thus studies that utilize the relatively high frequency portion of the broadband seismic spectrum may hold hope in elucidating such details.

As we have mentioned earlier, our simulations go far beyond conditions that can be experimentally verified, and we can identify different sources of uncertainties in our results. Because of the uncertainty associated with material parameters of lower mantle minerals, we expect a wide variability of possible mantle models at all scales. On the macroscopic scale, many parameter sets were explored [19], and it appears that the expected first-order deformational patterns in the lower mantle are not strongly sensitive to input parameters. Therefore, we propose that the parameters used in this study are representative of most convection models and do not expect the strain evolution to change appreciably as material and convection parameters are

varied. Similarly elastic properties at lower mantle conditions will be further refined but we do not foresee major changes. The largest uncertainty lies in microscopic mechanisms. Slip systems for perovskite have been inferred from room temperature experiments and observations on analogs. If more systems become active at high temperature, this might change the detailed texture pattern, but not the overall strength of the lattice preferred orientation. We have discussed issues of relative strength and volume fractions of the components, the possibility of concentration of deformation in shear bands etc. and the need for experiments as well as more realistic models along lines used in metallurgy [91]. For texture development we relied on polycrystal plasticity and rotations produced by intracrystalline slip. If other mechanisms are also active, including diffusion and dynamic recrystallization, texture development is likely reduced.

5. Conclusions

In conclusion, the model presented here predicts strong textures and moderate and asymmetric P-wave anisotropy of 3–4% and ΔS wave polarization anisotropy of up to 7% in a subducting slab in the lower mantle. The pattern is confined to the slab and should be different in other regions of the lower mantle. Such predictions are consistent with seismic observations though detailed seismic evidence is scarce. The results of this study have also implications for anisotropy near the core–mantle boundary that we have not emphasized but where the model predicts large local variations in strain and thus texture and anisotropy. In the future the same model can be easily expanded to a three-dimensional geodynamic model that is in preparation and can incorporate new data on mechanisms and elastic properties, including those of the newly discovered postperovskite polymorph of MgSiO_3 , as they become available, thus advancing our understanding of the dynamics in a large segment of Earth's interior.

Acknowledgements

HRW is appreciative for hospitality at GFZ Potsdam, where part of this work was done and for support by CDAC, NSF (EAR 0337006) and IGPP-LANL. SS acknowledges support from the Miller Institute at Berkeley. The work of AMc was supported by CSEDI EAR 9905601 and EJJ by NSF (EAR-0135119). Discussions with L. Stixrude and constructive comments by three reviewers were most useful.

References

- [1] J.P. Montagner, T. Tanimoto, Global anisotropy in the upper mantle inferred from the regionalization of phase velocities, *J. Geophys. Res.* 95 (1990) 4797–4819.
- [2] P.G. Silver, Seismic anisotropy beneath the continents: probing the depths of geology, *Annu. Rev. Earth Planet. Sci.* 24 (1996) 385–432.
- [3] J.M. Kendall, Seismic anisotropy in the boundary layers of the mantle, in: S. Karato, A.M. Forte, R.C. Liebermann, G. Masters, L. Stixrude (Eds.), *Earth's Deep Interior: Mineral Physics and Tomography From the Atomic to the Global Scale*, AGU, Washington D.C., 2000, pp. 133–159.
- [4] T. Lay, Q. Williams, E.J. Garnero, L. Kellogg, M.E. Wyssession, Seismic wave anisotropy in the D'' region and its implications, in: W.M., M. Gurnis, E. Knittle, B. Buffett (Eds.), *The Core–Mantle Boundary Region*, AGU, Washington D.C., 1998, pp. 229–318.
- [5] B. Romanowicz, X.-D. Li, J.J. Durek, Anisotropy in the inner core; could it be due to low-order convection? *Science* 274 (1996) 963–966.
- [6] X. Song, Anisotropy of the Earth's inner core, *Rev. Geophys.* 35 (1997) 297–313.
- [7] W. Ben Ismail, D. Mainprice, An olivine fabric database: an overview of upper mantle fabrics and seismic anisotropy, *Tectonophysics* 296 (1998) 145–157.
- [8] H.H. Hess, Seismic anisotropy of the uppermost mantle under oceans, *Nature* 203 (1964) 629.
- [9] D.K. Blackman, H.-R. Wenk, M.-J. Kendall, Seismic anisotropy in the upper mantle: 1. Factors that affect mineral texture and effective elastic properties, *Geochem. Geophys. Geosyst.* 3 (9) (2002) 8601, doi:10.1029/2001GC000248.
- [10] P.R. Dawson, H.-R. Wenk, Texturing of the upper mantle during convection, *Philos. Mag.*, A 80 (2000) 573–598.
- [11] H.-R. Wenk, J.R. Baumgardner, R.A. Lebensohn, C.N. Tomé, A convection model to explain anisotropy in the inner core, *J. Geophys. Res.* 105 (2000) 5663–5677.
- [12] T. Lay, E.J. Garnero, Core–mantle boundary structures and processes, in: R.S.J. Sparks, C.J. Hawkesworth (Eds.), *The State of the Planet: Frontiers and Challenges in Geophysics*, *Geophysical Monograph* 150, vol. 19IUGG, 2004, doi:10.1029/150GM04.
- [13] G. Masters, G. Laske, H. Bolton, A.M. Dziewonski, The relative behavior of shear velocity, bulk sound speed, and compressional velocity in the mantle: implications for chemical and thermal structure, in: S. Karato, A.M. Forte, R.C. Liebermann, G. Masters, L. Stixrude (Eds.), *Earth's Deep Interior: Mineral Physics and Tomography From the Atomic to the Global Scale*, AGU, Washington, D.C., 2000, pp. 63–87.
- [14] K.M. Fischer, Earth science: flow and fabric deep down, *Nature* 415 (2002) 745–748.
- [15] E. Ito, H. Sato, Aseismicity in the lower mantle by superplasticity of the descending slab, *Nature* 351 (1991) 140–141.
- [16] S.V. Panasyuk, B.H. Hager, A model of transformational superplasticity in the upper mantle, *Geophys. J. Int.* 133 (1998) 741–755.
- [17] G. Ranalli, B. Fischer, Diffusion creep, dislocation creep, and mantle rheology, *Phys. Earth planet. Inter.* 34 (1984) 77–84.
- [18] A.K. McNamara, P.E. van Keken, S.-I. Karato, Development of anisotropic structure by solid-state convection in the Earth's lower mantle, *Nature* 416 (2002) 310–314.
- [19] A.K. McNamara, P.E. van Keken, S.-I. Karato, Development of finite strain in the convecting lower mantle and its implications

- for seismic anisotropy, *J. Geophys. Res.* 108 (B5) (2003) 2230, doi:10.1029/2002JB001970.
- [20] U.R. Christensen, A.W. Hofmann, Segregation of subducted oceanic crust in the convecting mantle, *J. Geophys. Res.* 99 (1994) 19867–19884.
- [21] A.M. Jellinek, M. Manga, Links between long-lived hot spots, mantle plumes, D'' , and plate tectonics, *Rev. Geophys.* 42 (2004), doi:10.1029/2003RG000144.
- [22] L.H. Kellogg, B.H. Hager, R.D. van der Hilst, Compositional stratification in the deep mantle, *Science* 283 (1999) 1881–1884 (1).
- [23] A.K. McNamara, S. Zhong, The influence of thermochemical convection on the fixity of mantle plumes, *Earth Planet. Sci. Lett.* 222 (2004) 485–500.
- [24] N.L. Montague, L.H. Kellogg, M. Manga, High Rayleigh number thermo-chemical models of a dense boundary layer in D'' , *Geophys. Res. Lett.* 25 (1998) 2345–2348.
- [25] D. Yamazaki, S. Karato, Some mineral physics constraints on the rheology and geothermal structure of Earth's lower mantle, *Am. Mineral.* 86 (2001) 385–391.
- [26] S.-I. Karato, S. Zhang, H.-R. Wenk, Superplasticity in the Earth's lower mantle. Evidence from seismic anisotropy and rock physics, *Science* 270 (1995) 458–461.
- [27] G. Gottstein, Evolution of recrystallization textures — classical approaches and recent advances, *Mater. Sci. Forum* 408–412 (2002) 1–24.
- [28] H.-R. Wenk, G. Canova, Y. Brechet, L. Flandin, A deformation-based model for recrystallization of anisotropic materials, *Acta Mater.* 45 (1997) 3283–3296.
- [29] Y. Wang, W.B. Durham, I.C. Getting, D.J. Weidner, The deformation-DIA: a new apparatus for high temperature triaxial deformation to pressures up to 15 GPa, *Rev. Sci. Instrum.* 74 (2003) 3002–3011.
- [30] R.J. Hemley, H.-K. Mao, G. Shen, J. Badro, P. Gillet, M. Hanfland, D. Häusermann, X-ray imaging of stress and strain of diamond, iron, and tungsten at megabar pressures, *Science* 276 (1996) 1242–1245.
- [31] C. Meade, R. Jeanloz, Yield strength of MgO to 40 GPa, *J. Geophys. Res.* 93 (1998) 3261–3269.
- [32] S. Merkel, H.-R. Wenk, J. Shu, G. Shen, P. Gillet, H.K. Mao, R.J. Hemley, Deformation of MgO aggregates at pressures of the lower mantle, *J. Geophys. Res.* 107 (2002) 2271, doi:10.1029/2001JB000920.
- [33] F. Heidelbach, I. Stretton, F. Langenhorst, S. Machwell, Fabric evolution during high shear–strain deformation of magnesiowüstite, *J. Geophys. Res.* 108 (2003), doi:10.1029/2001JB001632.
- [34] I. Stretton, F. Heidelbach, S. Mackwell, F. Langenhorst, Dislocation creep of magnesiowüstite ($Mg_{0.8}Fe_{0.2}O$), *Earth Planet. Sci. Lett.* 194 (2001) 229–240.
- [35] D. Yamazaki, S. Karato, Shear deformation of (Mg,Fe)O: implications for seismic anisotropy in Earth's lower mantle, *Phys. Earth Planet. Inter.* 131 (2002) 251–267.
- [36] N.L. Carter, H.C. Heard, Temperature and rate-dependent deformation of halite, *Am. J. Sci.* 269 (1970) 193–249.
- [37] C.R. Miranda, S. Scandolo, Computational materials science meets geophysics: dislocations and slip planes of MgO, *Comput. Phys. Commun.* 169 (2005) 24–27.
- [38] P. Besson, J.P. Poirier, G.D. Price, Dislocations in $CaTiO_3$ perovskite deformed at high-temperature: a transmission electron microscopy study, *Phys. Chem. Miner.* 23 (1996) 337–344.
- [39] P. Cordier, Dislocations and slip systems of mantle minerals, in: S.-I. Karato, H.-R. Wenk (Eds.), *Plastic Deformation in Minerals and Rocks, Reviews in Mineralogy*, vol. 51 Mineralogical Society of America, 2002, pp. 137–179.
- [40] J.P. Poirier, S. Beauchesne, F. Guyot, Deformation mechanisms of crystals with perovskite structure, in: A. Navrotsky, D. Weidner (Eds.), *Perovskites, Monograph*, vol. 45A.G.U., Washington, D.C., 1991, pp. 119–123.
- [41] Z.C. Wang, S. Karato, K. Fujino, High temperature creep of single crystal strontium titanate ($SrTiO_3$) — a contribution to creep systematics in perovskites, *Phys. Earth Planet. Inter.* 79 (1993) 299–312.
- [42] K. Wright, G.D. Price, J.P. Poirier, High-temperature creep of the perovskite $CaTiO_3$ and $NaNbO_3$, *Phys. Earth Planet. Inter.* 74 (1992) 9–22.
- [43] P. Cordier, T. Ungar, L. Zsoldos, G. Tichy, Dislocation creep in $MgSiO_3$ perovskite at conditions of the Earth's uppermost mantle, *Nature* 428 (2004) 837–840.
- [44] H.-R. Wenk, I. Lonardelli, J. Pehl, J. Devine, V. Prakapenka, G. Shen, H.-K. Mao, In situ observation of texture development in olivine, ringwoodite, magnesiowüstite and silicate perovskite at high pressure, *Earth Planet. Sci. Lett.* 226 (2004) 507–519.
- [45] H.-R. Wenk, I. Lonardelli, S. Merkel, L. Miyagi, J. Pehl, S. Speziale, C.E. Tommaso, Diamond anvil deformation experiments in radial diffraction geometry. *J. Phys. Condens. Matter* (in press).
- [46] J.P. Brodholt, A.R. Oganov, G.D. Price, Computational mineral physics and the physical properties of perovskite, *Philos. Trans. R. Soc. Lond. Ser. A: Math. Phys. Sci.* 360 (2002) 2507–2520.
- [47] A.R. Oganov, J.P. Brodholt, G.D. Price, The elastic constants of $MgSiO_3$ perovskite at pressures and temperatures of the earth's mantle, *Nature* 411 (2001) 934–937.
- [48] R.M. Wentzcovitch, B.B. Karki, M. Cococcioni, S. de Gironcoli, Thermoelastic properties of $MgSiO_3$ -perovskite: insights on the nature of the Earth's lower mantle, *Phys. Rev. Lett.* 92 (2004), doi:10.1103/PhysRevLett92.018501.
- [49] J.S. Sweeney, D.L. Heinz, Laser heating through a diamond anvil cell: melting at high pressure, in: M.H. Manghnani, T. Yagi (Eds.), *Properties of Earth and Planetary Materials at High Pressure and Temperature*, AGU, Washington, D.C., 1998, pp. 197–213.
- [50] A. Zerr, R. Boehler, Melting of (Mg,Fe)SiO₃-perovskite to 625 kilobars: indication of high melting temperature in the lower mantle, *Science* 262 (1993) 553–555.
- [51] J. Chen, D. Weidner, M. Vaughan, The strength of Mg(0.9)Fe(0.1)SiO₃ perovskite at high pressure and temperature, *Nature* 419 (2002) 824–826.
- [52] G. Chen, R.C. Liebermann, D.J. Weidner, Elasticity of single-crystal MgO to 8 Gigapascals and 1600 Kelvin, *Science* 280 (1998) 1913–1916.
- [53] H.A. Spetzler, Equation of state of polycrystalline and single-crystal MgO to 8 kilobars and 800 K, *J. Geophys. Res.* 75 (1970) 2073–2087.
- [54] I. Jackson, H. Niesler, The elasticity of periclase to 3 GPa and some geophysical implications, in: S. Akimoto, M.H. Manghnani (Eds.), *High Pressure Research in Geophysics*, Center for Acad. Publ., Tokyo, Japan, 1982, pp. 93–113.
- [55] S.V. Sinogeikin, J.D. Bass, Single-crystal elasticity of pyrope and MgO to 20 GPa by Brillouin scattering in the diamond anvil cell, *Phys. Earth Planet. Inter.* 120 (2000) 43–62.
- [56] A. Yoneda, Pressure derivatives of elastic constants of single crystal MgO and $MgAl_2O_4$, *J. Phys. Earth* 38 (1990) 19–55.

- [57] C.S. Zha, H.K. Mao, R.J. Hemley, Elasticity of MgO and a primary pressure scale to 55 GPa, *Proc. Natl. Acad. Sci.* 97 (2000) 13494–13499.
- [58] D.G. Isaak, O.L. Anderson, T. Goto, Measured elastic modulus of single-crystal MgO up to 1800 K, *Phys. Chem. Miner.* 16 (1989) 704–713.
- [59] S.V. Sinogeikin, J. Zhang, J.D. Bass, Elasticity of single crystal and polycrystalline MgSiO₃ perovskite by Brillouin spectroscopy, *Geophys. Res. Lett.* 31 (2004), doi:10.1029/GL019559.
- [60] A. Yeganeh-Haeri, Synthesis and re-investigation of the elastic properties of single-crystal magnesium silicate perovskite, *Phys. Earth Planet. Inter.* 87 (1994) 111–121.
- [61] B. Li, J. Zhang, Pressure and temperature dependence of elastic wave velocity of MgSiO₃ perovskite and the composition of the lower mantle, *Phys. Earth Planet. Inter.* 151 (2005) 143–154.
- [62] Y.D. Sinelnikov, G. Chen, D.R. Neuville, M.T. Vaughan, R.C. Liebermann, Ultrasonic shear velocities of MgSiO₃-perovskite at 8 GPa and 800 K and lower mantle composition, *Science* 281 (1998) 677–679.
- [63] B.B. Karki, R.M. Wentzcovitch, S. de Gironcoli, S. Baroni, First principles determination of elastic anisotropy and wave velocities of MgO at lower mantle conditions, *Science* 286 (1999) 1705–1709.
- [64] B.B. Karki, R.M. Wentzcovitch, S. de Gironcoli, S. Baroni, High-pressure lattice dynamics and thermoelasticity of MgO, *Phys. Rev., B* 61 (2000) 8793–8800.
- [65] A.R. Oganov, P.I. Dorogokupets, Intrinsic anharmonicity in equation of state and thermodynamics of solids, *J. Phys., Condens. Matter* 16 (2001) 1351–1360.
- [66] L. Stixrude, C. Lithgow-Bertelloni, Mineralogy and elasticity of the oceanic upper mantle: origin of the low velocity zone, *J. Geophys. Res.* 110 (2005), doi:10.1029/2004JB002965.
- [67] S.D. Jacobsen, H.J. Reichmann, H.A. Spetzler, S.J. Mackwell, J. R. Smith, R.J. Angel, R.J.C.A. McCammon, Structure and elasticity of single-crystal (Mg,Fe)O and a new method of generating shear waves for gigahertz ultrasonic interferometry, *J. Geophys. Res.* 107 (2002), doi:10.1029/JB000490.
- [68] T. Gasparik, Phase relations in the transition zone, *J. Geophys. Res.* 95 (1990) 15751–15769.
- [69] B. Kiefer, L. Stixrude, R.M. Wentzcovitch, Elasticity of (Mg,Fe) SiO₃ at high pressures, *Geophys. Res. Lett.* 29 (2002), doi:10.1029/2002GL014683.
- [70] J. Badro, J.-P. Rueff, G. Vankó, G. Monaco, G. Fiquet, F. Guyot, Electronic transition in perovskite: possible nonconvecting layers in the lower mantle, *Science* 305 (2004) 383–386.
- [71] J.-F. Lin, V.V. Struzhkin, S.D. Jacobsen, M. Hu, P. Chow, J. Kung, H. Liu, H.-K. Mao, R.J. Hemley, Spin transition of iron in magnesiowüstite in the lower mantle, *Nature* 436 (2005) 377–380.
- [72] W. Sturhahn, J.M. Jackson, J.-F. Lin, The spin state of iron in minerals of Earth's lower mantle, *Geophys. Res. Lett.* 32 (2005), doi:10.1029/2005GL022802.
- [73] R.A. Lebensohn, C.N. Tomé, A self-consistent anisotropic approach for the simulation of plastic deformation and texture development of polycrystals — application to zirconium alloys, *Acta Metall. Mater.* 41 (1993) 2611–2624.
- [74] H.-R. Wenk, A voyage through the deformed Earth with the self-consistent model, *Model. Mater. Sci. Eng.* 7 (1999) 699–722.
- [75] G.R. Canova, H.-R. Wenk, A. Molinari, Deformation modelling of multiphase polycrystals: case of a quartz–mica aggregate, *Acta Metall.* 40 (1992) 1519–1530.
- [76] S. Matthies, M. Humbert, The realization of the concept of the geometric mean for calculating physical constants of polycrystalline materials, *Phys. Status Solidi, B Basic Res.* 177 (1993) K47–K50.
- [77] H.-R. Wenk, S. Matthies, J. Donovan, D. Chateigner, BEAR-TEX, a Windows-based program system for quantitative texture analysis, *J. Appl. Cryst.* 31 (1998) 262–269.
- [78] C.S. Zha, T.S. Duffy, R.T. Downs, H.K. Mao, R.J. Hemley, Brillouin scattering and X-ray diffraction of San Carlos olivine: direct pressure determination to 32 GPa, *Earth Planet. Sci. Lett.* 159 (1998) 25–33.
- [79] K. Madi, S. Forest, P. Cordier, M. Boussuge, Numerical study of creep in two-phase aggregates with a large viscosity contrast: implications for the rheology of the lower mantle, *Earth Planet. Sci. Lett.* 237 (2005) 223–238.
- [80] J. Ritsema, Evidence for shear velocity anisotropy in the lowermost mantle beneath the Indian Ocean, *Geophys. Res. Lett.* 27 (2000) 1041–1044.
- [81] L. Vinnik, L. Breger, B. Romanowicz, Anisotropic structures at the base of the earth's mantle, *Nature* 393 (1998) 564–567.
- [82] M.M. Moore, E.J. Garnero, T. Lay, Q. Williams, Shear wave splitting and waveform complexity for lowermost mantle structures with low-velocity lamellae and transverse isotropy, *J. Geophys. Res.* 109 (2004) B02319, doi:10.1029/2003JB002546.
- [83] M.J. Fouch, K.M. Fisher, M.E. Wysession, Lowermost mantle anisotropy beneath the Pacific: imaging the source of the Hawaiian plume, *Earth Planet. Sci. Lett.* 190 (2001) 167–180.
- [84] E.J. Garnero, V. Maupin, T. Lay, M.J. Fouch, Variable azimuthal anisotropy in Earth's lowermost mantle, *Science* 306 (2004) 5694.
- [85] M. Panning, B. Romanowicz, Inferences on flow at the base of earth's mantle based on seismic anisotropy, *Science* 303 (2004) 351–353.
- [86] E.J. Garnero, M.M. Moore, T. Lay, M. Fouch, Isotropy or weak vertical transverse isotropy in D'' beneath the Atlantic Ocean, *J. Geophys. Res.* 109 (2004), doi:10.1029/2004JB003004.
- [87] M. Murakami, K. Hirose, K. Kawamura, N. Sata, Y. Ohishi, Post-perovskite phase transition in MgSiO₃, *Science* 304 (2004) 855–859.
- [88] A.R. Oganov, S. Ono, Theoretical and experimental evidence for a post-perovskite phase of MgSiO₃ in Earth's D'' layer, *Nature* 430 (2004) 445–448.
- [89] J. Hernlund, C. Thomas, P. Tackley, Phase boundary double-crossing and partial melting in Earth's deepest mantle, *Nature* 434 (2005) 882–886.
- [90] S. Merkel, A. Kubo, L. Miyagi, S. Speziale, T.S. Duffy, H.-K. Mao, H.-R. Wenk, Plastic deformation of MgGeO₃ post-perovskite at lower mantle pressures, *Science* 311 (2006) 644–646.
- [91] D.P. Miki, P.R. Dawson, Polycrystal plasticity modeling of intracrystalline boundary textures, *Acta Mater.* 47 (1999) 1355–1369.